Journal of Hydroscience and Hydraulic Engineering
Vol. 27, No.1 May, 2009, 23-35

NUMERICAL PREDICTION FOR FLUID FORCES ACTING ON 3D COMPLICATED-SHAPED OBJECTS IN FREE-SURFACE FLOWS

By

Satoru Ushijima

Department of Civil and Earth Resources Engineering, Kyoto University, Kyoto-shi, 615-8540, Japan

Norimasa Yoshikawa

Department of Civil and Earth Resources Engineering, Kyoto University, Kyoto-shi, 615-8540, Japan

and

Nozomu Yoneyama

Disaster Prevention Research Inst., Kyoto University, Kyoto, Japan

SYNOPSIS

The focus of this paper is on the applicability of the computational method used to predict the fluid forces acting on the complicated-shaped solid objects included in free-surface flows. The computational method, MICS, enables us to predict the fluid forces on the basis of the pressure and viscous terms of the governing equations for incompressible multiphase fields. A solid object is represented by multiple tetrahedron elements and their volume fractions included in a fluid-cell are evaluated with a tetrahedron sub-cell method. The predicted results were compared with the measured fluid forces against a wave breaking block placed in free-surface flows. As a result, it has been demonstrated that the computational method allows us to predict the difference of the fluid forces according to the block attitudes and the relationship between the fluid forces and wave heights.

INTRODUCTION

According to the usual reports, the buildings and trees located along rivers and near coastal regions are sometimes destroyed by flooded flows and tsunamis. In addition, collisions and entrapments of debris cause other disasters in many cases. In order to assess such phenomena, it is necessary to understand accurately the fluid forces which act on the complicated-shaped objects exposed to free-surface flows. While many experimental investigations have been made to evaluate the fluid forces of the free-surface flows in various conditions as shown in (1) and (2), there have been few computational methods that can be applied to such complicated hydraulics conditions. Thus, in the present study, a numerical method is developed to predict the fluid forces acting on the arbitrarily-shaped objects in free-surface flows and its applicability is discussed through the comparisons with experimental results.

In the numerical methods which evaluate fluid forces, the boundary-fitted coordinates and unstructured meshes are generally used to represent the geometries of the objects and that the normal and tangential stresses are integrated on the surfaces. It has been shown that these methods are applicable to the evaluation of the fluid

forces against the objects that have relatively simple shapes, such as cylinders and spheres placed in the flows without free surfaces.

On the other hand, it is necessary to deal with complicated-shaped objects as well as the effects of free-surface motions in the actual problems. In addition, since the movements and collisions of the objects have to be taken into account, it is difficult to distinguish the boundaries between the fluids and objects using grid systems and to apply the surface integration of the stresses as done in the usual numerical methods. Therefore, the computational methods, which treat the free-surface flows including solid objects as the multiphase fields like (3).are effective for such complicated problems. The MICS (4) is one of the computational methods for multiphase fields and its applicability has been demonstrated for the movements of the three-dimensional objects falling in water and the floating blocks transported by wave-induced flows with collisions (5).

In the present study, the predicted fluid forces with MICS are investigated quantitatively with the experimental results. The fluid forces acting on a four-leg wave-breaking block due to wave-induced flows are measured with strain gages in an experimental flume. The experimental values are compared with the predicted results and the applicability of MICS is discussed.

NUMERICAL PROCEDURES

Basic equations for multiphase fields

The multiphase field consisting of gas, liquid and solid phases is treated as a mixture of fluids Ω, which is the collection of the immiscible and incompressible fluids Ω_i, as shown in Fig.1. The fluid components Ω_i in Fig.1 have different physical properties equivalent to the corresponding phases. This treatment enables us to deal with the free-surface motions and the fluid forces which act on the complicated-shaped objects easily and accurately.

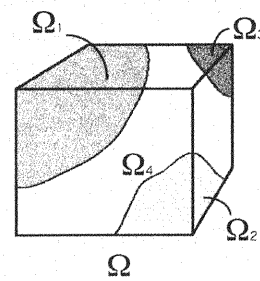

Fig. 1 Mixture of immiscible and incompressible fluids

The mass-conservation equations in the Eulerian and Lagrangian forms for the fluid mixture Ω are given as follows:

$$\sum_k \int_{\Omega_k} \left[\frac{\partial \rho_k}{\partial t} + \frac{\partial}{\partial x_j}(\rho_k u_{k,j}) \right] d\Omega = 0 \tag{1}$$

$$\sum_k \int_{\Omega_k} \left(\frac{\partial \rho_k}{\partial t} + u_{k,j} \frac{\partial \rho_k}{\partial x_j} \right) d\Omega = 0 \tag{2}$$

where ρ_k and $u_{k,i}$ are density and velocity component in the x_i direction of the fluid-k respectively. From the above two equations, the incompressible condition is derived as

$$\sum_k \int_{\Omega_k} \frac{\partial u_{k,i}}{\partial x_i} d\Omega = 0 \tag{3}$$

The momentum equation for Ω is given by

$$\sum_k \int_{\Omega_k} \left[\frac{\partial}{\partial t}(\rho_k u_{k,i}) + \frac{\partial}{\partial x_j}(\rho_k u_{k,i} u_{k,j}) \right] d\Omega = \sum_k \int_{\Omega_k} \left[\frac{\partial \tau_{k,ij}}{\partial x_j} + \rho_k f_i \right] d\Omega + \int_{\partial I} F_{s,i}\, dS \tag{4}$$

where f_i is the acceleration component of the external force and the second term on the right-hand side of Eq.4 means the surface integration of the surface tension $F_{s,i}$ acting in the x_i direction. The stress $\tau_{k,ij}$ is defined as

$$\tau_{k,ij} = -p_k \delta_{ij} + \mu_k e_{k,ij} \tag{5}$$

where δ_{ij}, p_k, μ_k, $e_{k,ij}$ are the Kronecker delta, pressure, viscous coefficient and deformation tensor of fluid-k, respectively.

Assuming that the volume of Ω is sufficiently small, a certain variable $\phi_k^{'}(t, \boldsymbol{x})$ in each fluid is approximated as its spatially-representative value $\phi_k(t)$ as follows:

$$\int_{\Omega_k} \phi_k^{'}(t, \boldsymbol{x})\, d\Omega \approx \int_{\Omega_k} \phi_k(t)\, d\Omega = \Omega_k \phi_k(t) \tag{6}$$

Based on this relationship, Eq.1 is rewritten as

$$\frac{\partial \rho}{\partial t} + \frac{\partial}{\partial x_j}(\rho u_j) = 0 \tag{7}$$

where ρ and u_i are volume-average density and mass-average velocity component defined as:

$$\rho = \frac{\sum_k \Omega_k \rho_k}{\Omega}, \qquad u_i = \frac{\sum_k \Omega_k \rho_k u_{k,i}}{\Omega \rho} \tag{8}$$

Similarly, with the relationship $u_{k,i} = u_i + \tilde{u}_{k,i}$, Eq.2 is written as

$$\frac{\partial \rho}{\partial t} + u_j \frac{\partial \rho}{\partial x_j} + \frac{1}{\Omega} \sum_k \Omega_k \tilde{u}_{k,j} \frac{\partial \rho_k}{\partial x_j} = 0 \tag{9}$$

Since $\tilde{u}_{k,j}$ means the difference of velocities between the fluid mixture and each fluid components, the third term on the left-hand side of Eq.9 is negligible in case that the resolution of fluid cell is sufficient. Thus, the following incompressible condition is derived from Eqs.7 and 9:

$$\frac{\partial u_j}{\partial x_j} = 0 \tag{10}$$

With the similar procedures, Eq.4 is rewritten as

$$\frac{\partial}{\partial t}(\rho u_i) + \frac{\partial}{\partial x_j}(\rho u_i u_j) = \rho f_i + \rho f_{s,i} + \frac{\partial \tau_{i,j}}{\partial x_j} - \frac{1}{\Omega} \frac{\partial}{\partial x_j} \sum_k \Omega_k \rho_k \tilde{u}_{k,i} \tilde{u}_{k,j} \tag{11}$$

In Eq.11, as proposed by a CSF model (6), the surface force is treated as

$$\int_{\partial I} F_{s,i}\, dS = \rho f_{s,i} \Omega \tag{12}$$

This relationship means that the surface force is transformed to the body force. With the same treatment for the third term of Eq.9, the fourth term of Eq.11 can be neglected. Putting the third term on the right-hand-side of Eq.11 D_i, it is written with Eq.5 as

$$D_i = -\frac{\partial p}{\partial x_i} + \frac{\partial}{\partial x_j} \left[\frac{\partial}{\partial x_j}(\mu u_i) + \frac{\partial}{\partial x_i}(\mu u_j) \right] \tag{13}$$

where p and μ are volume-average pressure and viscous coefficient defined as follows:

$$p = \frac{\sum_k \Omega_k p_k}{\Omega}, \qquad \mu = \frac{\sum_k \Omega_k \mu_k}{\Omega} \tag{14}$$

Finally, assuming that the non-linear term $\tilde{u}_{k,i}\tilde{u}_{k,j}$ in Eq.11 and the surface tension are negligible, the conservative form of the momentum equation is derived as

$$\frac{\partial u_i}{\partial t} + \frac{\partial}{\partial x_j}(u_i u_j) = f_i - \frac{1}{\rho}\frac{\partial p}{\partial x_i} + \frac{1}{\rho}\frac{\partial}{\partial x_j}\left[\frac{\partial}{\partial x_j}(\mu u_i) + \frac{\partial}{\partial x_i}(\mu u_j)\right] \tag{15}$$

The governing equations of the MICS consist of Eqs.7, 10 and 15.

Discretization and computational method

The discretized governing equations of the fluid-mixture are solved after determining the volume-average physical properties by means of the tetrahedron sub-cell method, which will be described in the next section. The three-dimensional velocity components u_i and the pressure variable p of the discretized equations are defined on the collocated grid points in the fluid-cell.

The numerical procedures of the incompressible fluid-mixture in a MAC-type method consist of three stages; prediction, pressure-computation and correction stages. At the prediction stage, the tentative velocity components u_i^* are calculated at the center of the fluid-cells with a finite-volume method. In this procedure, Eq.15 is discretized with the C-ISMAC method proposed by Ushijima et al. (7), which is based on the implicit SMAC method (8) that allows us to decrease computational time without decreasing numerical accuracy. The equation discretized with respect to time by using the C-ISMAC method is given by

$$\begin{aligned}\frac{u_i^* - u_i^n}{\Delta t} &= f_i - \frac{1}{\rho}\frac{\partial p^n}{\partial x_i} - \alpha\frac{\partial}{\partial x_j}(u_i^* u_j^n) - (1-\alpha)\frac{\partial}{\partial x_j}(u_i^n u_j^n) \\ &+ \frac{\beta}{\rho}\frac{\partial}{\partial x_j}\left[\frac{\partial}{\partial x_j}(\mu u_i^*) + \frac{\partial}{\partial x_i}(\mu u_j^*)\right] + \frac{1-\beta}{\rho}\frac{\partial}{\partial x_j}\left[\frac{\partial}{\partial x_j}(\mu u_i^n) + \frac{\partial}{\partial x_i}(\mu u_j^n)\right]\end{aligned} \tag{16}$$

where α and β are parameters whose ranges are $0 \leq \alpha, \beta \leq 1$. With the following relationship,

$$u_i^* = u_i^n + \tilde{u}_i \tag{17}$$

Eq.16 is transformed to the following equation:

$$\begin{aligned}&\frac{\tilde{u}_i}{\Delta t} + \alpha\frac{\partial}{\partial x_j}(\tilde{u}_i u_j^n) - \frac{\beta}{\rho}\frac{\partial}{\partial x_j}\left[\frac{\partial}{\partial x_j}(\mu\tilde{u}_i) + \frac{\partial}{\partial x_i}(\mu\tilde{u}_j)\right] \\ &= f_i - \frac{1}{\rho}\frac{\partial p^n}{\partial x_i} - \frac{\partial}{\partial x_j}(u_i^n u_j^n) + \frac{1}{\rho}\frac{\partial}{\partial x_j}\left[\frac{\partial}{\partial x_j}(\mu u_i^n) + \frac{\partial}{\partial x_i}(\mu u_j^n)\right]\end{aligned} \tag{18}$$

where $\tilde{u}_i$ becomes nearly zero when the flow field is almost steady or the time-scale of the flow field is sufficiently larger than the time increment Δt. Thus, we can apply a simple first-order spatial discretization method to the left-hand side of Eq.18, while some higher-order schemes to the right-hand side. The convection terms are evaluated with a fifth-order conservation FVM-QSI scheme (9) and numerical oscillations are removed by a flux-control method (9). The C-ISMAC method enables us to derive the simultaneous equation system easily from the implicit form of the left-hand side of Eq.18 as well as to preserve numerical accuracy by applying the higher-order schemes to the explicit form on the right-hand side Eq.18.

After solving the equation system of $\tilde{u}_i$, which is derived from the discretized equation of Eq.18, we obtain u_i^* with Eq.17. The u_i^* derived at the center of the fluid-cell is then spatially interpolated on the cell boundary. Before this interpolation, the pressure-gradient term evaluated at the cell center is removed from u_i^* in order to prevent pressure oscillation as

$$\hat{u}_i = u_i^* + \frac{1}{\rho}\frac{\partial p^n}{\partial x_i}\Delta t \tag{19}$$

The cell-center velocity $\hat{u}_i$, which does not include the pressure-gradient term, is spatially interpolated on the cell boundaries by a suitable function f_b. After completing this procedure, the pressure-gradient terms that are estimated on the cell boundaries are added to the interpolated velocity, $f_b(\hat{u}_i)$. Thus, we obtain the cell-boundary velocity component $u_{b,i}$ as follows:

$$u_{b,i} = f_b(\hat{u}_i) - \frac{1}{\rho}\frac{\partial p^n}{\partial x_i}\bigg|_b \Delta t \tag{20}$$

The velocity component $u_{b,i}^{n+1}$ at $n+1$ time-step is defined by

$$u_{b,i}^{n+1} = f_b(\hat{u}_i) - \frac{1}{\rho}\frac{\partial p^{n+1}}{\partial x_i}\bigg|_b \Delta t \tag{21}$$

Subtracting Eq.20 from Eq.21, we have

$$u_{b,i}^{n+1} = u_{b,i} - \frac{1}{\rho}\frac{\partial \phi}{\partial x_i}\Delta t \tag{22}$$

where $\phi = p^{n+1} - p^n$. Substitution of Eq.22 into the incompressible condition given by Eq.10 that is estimated at $n+1$ time-step yields the following equation of ϕ :

$$\frac{\partial}{\partial x_i}\left(\frac{1}{\rho}\frac{\partial \phi^k}{\partial x_i}\right) = \frac{1}{\Delta t}\frac{\partial u_{b,i}}{\partial x_i} \equiv \frac{D}{\Delta t} \tag{23}$$

At the pressure-computation stage, Eq.23 is solved by using the C-HSMAC method proposed by Ushijima et al. (10). The C-HSMAC method enables us to obtain the pressure and cell-boundary velocity components, which satisfy the incompressible condition $|D| < \epsilon_D$ in each computational cell, where ϵ_D is a given threshold. While the final results of the C-HSMAC method are similar to those of the SOLA or HSMAC method (11), it has been proved that the computational efficiency of the C-HSMAC method is largely improved as shown in (4). The relationships used in the C-HSMAC method are given by

$$\frac{\partial}{\partial x_i}\left(\frac{1}{\rho}\frac{\partial \phi}{\partial x_i}\right) = \frac{D^k}{\Delta t} \tag{24}$$

$$p^{k+1} = p^k + \phi \tag{25}$$

$$u_{b,i}^{k+1} = u_{b,i}^k - \frac{\Delta t}{\rho}\frac{\partial \phi}{\partial x_i} \tag{26}$$

where the superscript k denotes the iteration step-number of the C-HSMAC method. The initial values of $u_{b,i}^k$ and p^k are $u_{b,i}$ given by Eq.20 and p^n respectively.

The discretization of Eq.24 yields simultaneous linear equation system of ϕ, which is solved with the BiCGSTAB method (12). The iterative computation using the above three equations is completed when $|D| < \epsilon_D$ is satisfied in all fluid-cells.

Tetrahedron sub-cell method

As shown in the derivation of the governing equations, the physical values of the mixture of fluids need to be determined for each fluid-cell. Since the fluid-cell is based on the Eulerian grid which is fixed in the space, the volume-average physical value ψ in the fluid-cell is estimated with the following equation:

$$\psi = (1-f)\psi_g + \left(f - \sum_{P_k \in C}\alpha_k\right)\psi_l + \sum_{P_k \in C}\alpha_k\psi_{bk} \tag{27}$$

where ψ_g and ψ_l are physical values in gas and liquid phases respectively and ψ_{bk} is that of the object$-k$. The volume fraction of liquid and solid phases in a fluid-cell is given by f and the fraction of the solid part is defined by α_k. The fraction α_k is approximated with a tetrahedron sub-cell method, as shown in Fig.2. As shown later, a solid object is represented by multiple tetrahedron elements. When the element is completely included in a single fluid-cell as shown in Fig.2 (a), α_k is easily determined as the volume of the element. In contrast, when the element is included in multiple fluid-cells as shown in Fig.2 (b), a fluid-cell is divided into multiple sub-cells and α_k is determined from the number of the sub-cells included in the element. The accuracy of the sub-cell method can be improved by using the smaller sub-cells.

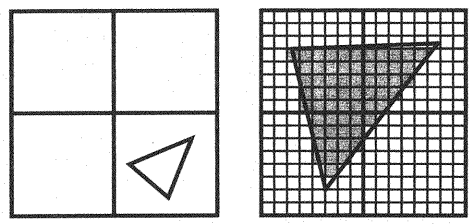

(a) a single fluid-cell (b) multiple fluid-cells

Fig. 2 Sub-cell method (thick grid lines stand for fluid-cell and thin lines in (b) indicate sub-cells)

T-type solid model and fluid forces acting on objects

A solid object in the flow is numerically represented using a T-type solid model. The object surface model, created with a CAD software, is divided into multiple tetrahedron elements with a three-dimensional mesh generator. Compared with the "sphere-connected model", which represents an object with multiple sphere elements, T-type model has an advantage in that its approximations of volume, mass and inertia tensors are more accurate.

The fluid forces acting on the objects are calculated with the pressure and viscous terms obtained from the computational results of Eq.15:

$$F_{Cki} = \alpha_k \sigma_k \Delta C \cdot \left[-\frac{1}{\rho}\frac{\partial p}{\partial x_i} + \frac{1}{\rho}\frac{\partial}{\partial x_j}\left\{ \frac{\partial}{\partial x_j}(\mu u_i) + \frac{\partial}{\partial x_i}(\mu u_j) \right\} \right] \tag{28}$$

where F_{Cki} is the x_i component of $\boldsymbol{F}_{Ck}$, which is the fluid force vector acting on the colored area of the object$-k$ shown in Fig.3 included in a fluid-cell C. The component F_{Cki} is evaluated from Eq.28 with the volume of a fluid-cell ΔC, density of the body σ_k and volume fraction α_k calculated with the tetrahedron sub-cell method.

HYDRAULIC EXPERIMENTS AND APPLICABILITY OF THE PREDICTION METHOD

Hydraulic experiments to measure fluid forces acting on arbitrarily-shaped objects

The fluid forces acting on an arbitrarily-shaped object, a four-leg wave-breaking block (tetra-pod), were measured in a flume with a wave generator. The schematic view of the experimental flume is shown in Fig.4. The wave generator, which is a flat plate fixed to an electric slider controlled by a PC, is set up on the left side of the flume. A box is fixed on the right side of the flume, on which the generated waves become free-surface flows. On

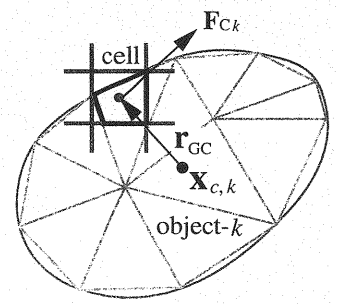

Fig. 3 Fluid force acting on a portion of tetrahedron element in a fluid-cell

the top surface of the box, a target block model is supported by a steel plate. The bottom of the block model is located about 4 mm above the top of the box, so that no friction forces can arise between them.

As shown in Fig.4, the length of the flume $(L_1 + L_2)$ is 1.4 m. The length and height of the box L_2 is 0.7 m and 0.1 m, respectively. The width of the flume and the box B are the same and 0.19m. The initial static water depth h_0 and the height of the box h_b were 0.104m and 0.1 m respectively. In this initial condition, the water level is located 4 mm above the top of the box, which is identical to the heights of the bottom of the block model. The block model, whose height is about 56 mm, is made of hard rubber and its specific gravity is 2.14. In these experiments, the center of the block model is located about 0.1m from the left edge of the box.

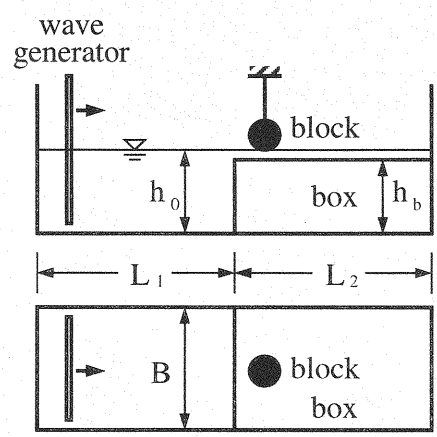

Fig. 4 Experimental flume with a wave generator
(top = side view, bottom = plane view)

Fig.5 (a) shows the block model with its supporting plate. Four strain gages were attached to the top of the supporting plate to measure the fluid forces acting on the block model. The output data of the strain gages were taken through the sensor interfaces and stored in a PC. The numerical filters, which were determined from the free-oscillation of the block model, were applied to the obtained data in order to remove the effects of its natural frequencies.

The water depth h_m is defined as the maximum water depth created by the waves at 0.1 m on the left side of the front edge of the box. Two attitudes were defined for the block model as shown in Fig.5 (b). While one

leg of the block model faces on the wave generator in the attitude-A, it is set in the opposite direction in the attitude-B. Three conditions were set up with different h_m, 125, 135 and 147 mm, for two attitudes of the block model and fluid forces were measured in all cases.

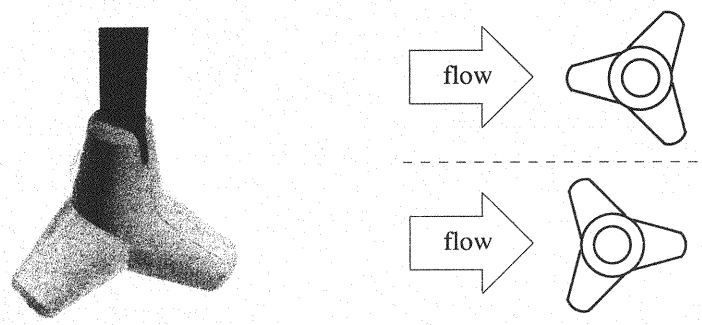

(a) Block model (photo)

(b) Attitudes of block model

Fig. 5 Block model and its attitude

Computational conditions

In the computations, $140 \times 38 \times 50$ fluid-cells were set up for the water and air regions and time increment Δt was set at 1.0×10^{-2} sec. The initial computational conditions are the same as those of the experiments, in which the fluid velocity on the left side of the flume is identical to the speed of the wave-generating plate. The unsteady computations continue until the first wave passes through the block model, which is equivalent to 1.5 sec. The computational time for one unsteady calculation is about 40 minutes with a single CPU (Pentium4, 2.66GHz).

The solid-model used in the computations is shown Fig.6, which represents the block model used in the experiments. The solid-model consists of multiple tetrahedron elements which was created by means of a CAD software and a mesh generator. The number of the tetrahedron elements is 416 and that of their nodes is 152. The density of the solid model is the same as that of the actual block model. The number of the sub-cells is $5 \times 5 \times 5$ in each fluid-cell.

The kinematic viscosities of water and air are 1.0×10^{-6} and 1.0×10^{-5} m^2/s, respectively. Their densities are 1.0×10^3 and 1.0 kg/m^3 respectively in the computations.

Comparison between experiments and computations

Tab.1 shows the comparisons between experiments and computations for maximum water depth h_m. As shown in Tab.1, predicted h_m almost agrees with the experimental values. The definition of the conditions, H125, H135 and H147, are also indicated in Tab.1.

Table 1 Comparisons of h_m (unit : mm)

case	H125	H135	H147
experiments	125	135	147
computations	125	133	145

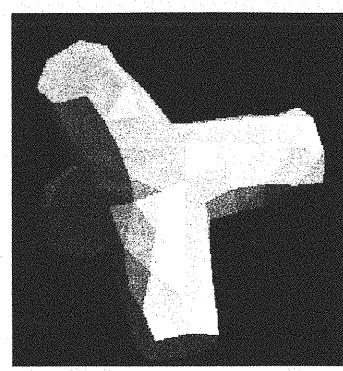

Fig. 6 Solid model used in computations

Fig.7 shows the time histories of the fluid forces F_w acting on the block model in H147. The predicted results are in agreement with the measured values.

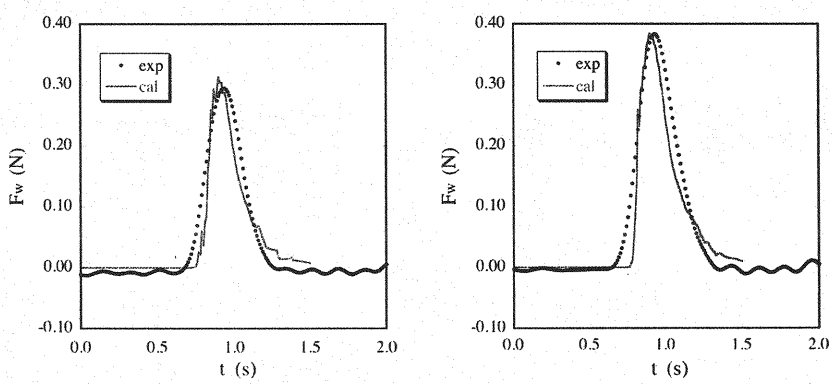

(a) attitude-A, case H147 (b) attitude-B, case H147

Fig. 7 Time histories of fluid force acting on block

The present measuring system enables us to obtain the fluid force component F_w only in the flow direction. As shown in Fig.7, the maximum fluid force of F_w in the attitude-B is larger than that of the attitude-A.

Fig.8 and Fig.9 show the computational results of the free-surface profiles around the block model. When the wave-induced flows collide with the block model, the water depth in front of the block becomes deeper than the depth behind the block. The same tendencies were observed in the experiments, while their quantitative values were not measured. It can be thought that the fluid forces against the block model consist of the static pressure due to the difference of the free-surface levels and the pressure distributions created by the vorticities behind the block. Since the high-level water area in front of the block model in the attitude-B is larger than the attitude-A as shown in Fig.8 and Fig.9. As a result, the static pressure is dominant in the attitude-B. This is probably one of the factors that make the maximum value of F_w in the attitude-B larger than the attitude-A.

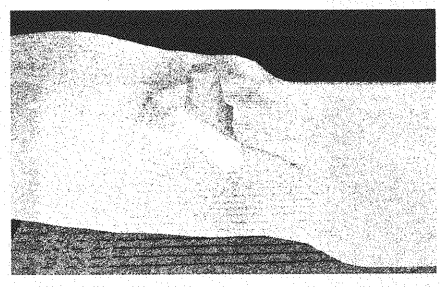

$t = 1.0$ (s)

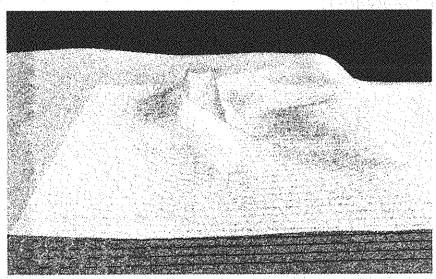

$t = 1.1$ (s)

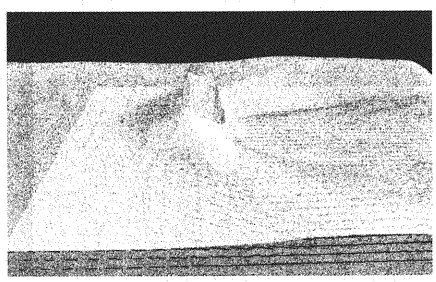

$t = 1.2$ (s)

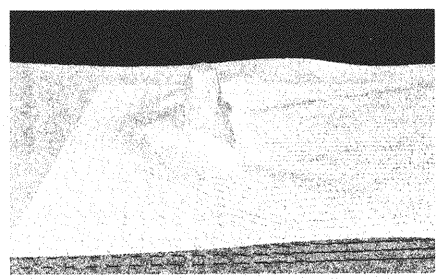

$t = 1.3$ (s)

Fig. 8 Predicted free-surface flows around block model (attitude-A, red lines = flow patterns near the box surface)

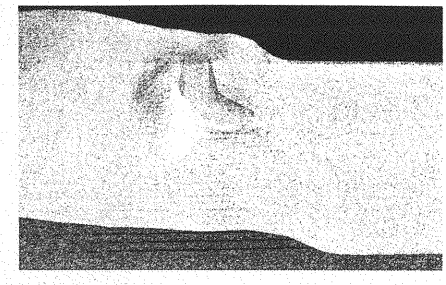

$t = 1.0$ (s)

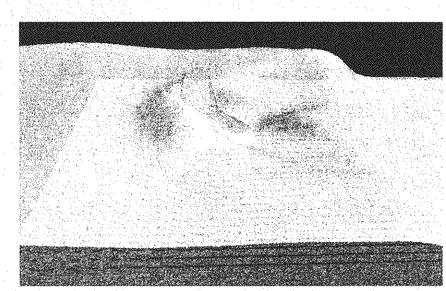

$t = 1.1$ (s)

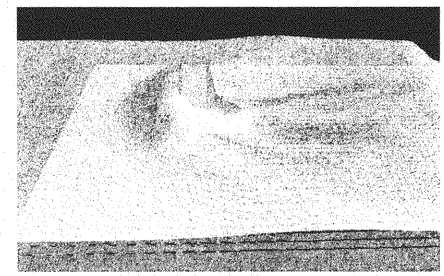

$t = 1.2$ (s)

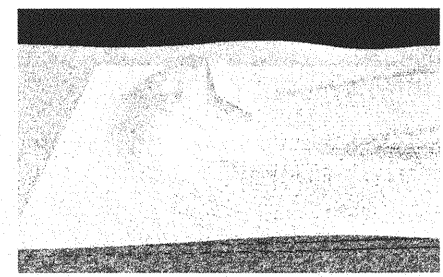

$t = 1.3$ (s)

Fig. 9 Predicted free-surface flows around block model (attitude-B, red lines = flow patterns near the box surface)

Fig.10 shows the relationship between maximum fluid forces F_{wm} acting on the block model and the water depths $w_h(= h_m - h_b)$ on the basis of the top surface of the box. It can be observed that F_{wm} increases with the increase of w_h and that the fluid forces in the attitude-B are larger than in the attitude-A in all cases. It is shown that these tendencies can be reasonably predicted with the present computational method.

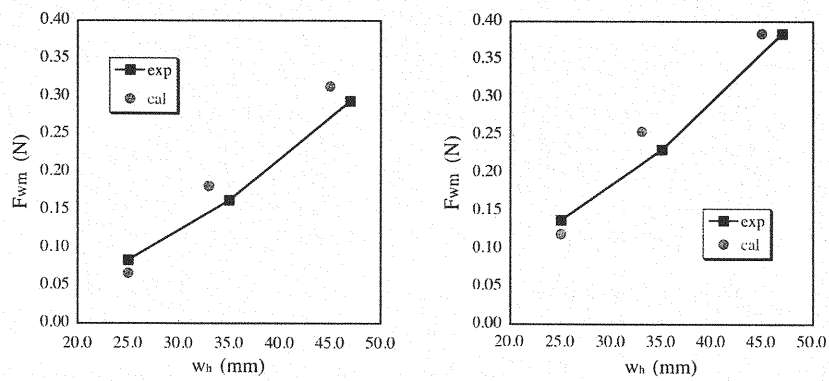

(a) Attitude-A (b) Attitude-B

Fig. 10 Relationship between maximum fluid forces F_{wm} and water depth w_h on box top surface ($w_h = h_m - h_b$)

CONCLUSIONS

A computational method for multiphase fields, MICS, was developed to predict the fluid forces of free-surface flows against arbitrarily-shaped objects and its applicability was confirmed through the comparisons with experimental results. In the MICS, the fluid forces are evaluated from the pressure and viscous terms of the governing equations for incompressible multiphase fields. A T-type solid model was introduced in MICS, in which an object is represented by multiple tetrahedron elements and the acting fluid forces are evaluated with a tetrahedron sub-cell method. The predicted results were compared with the measured fluid forces against a wave breaking block fixed in free-surface flows. As a result, it has been demonstrated that the computational method enables us to predict the difference of the fluid forces according to the block attitudes and the relationship between the fluid forces and wave heights.

REFERENCES

1. Shige-eda, M., Akiyama, J. and Ishihara, J.: Hydrodynamic forces acting on a submerged square pillar in sub- or super-critical flow, *Annu. J. Hydraulic Eng., JSCE*, Vol. 50, pp. 889–894, 2006.

2. Hayashi, K., Konno, M., Hamaguchi, K. and Abe, Y.: Flow-induced forces acting on a revetment block with large height relative to waterdepth of open-channel flows, *Annu. J. Hydraulic Eng., JSCE*, Vol. 50, pp. 859–864, 2006.

3. Xiao, F., Yabe, T., Ito, T. and Tajima, M.: An algorithm for simulating solid objects suspended in stratified flow, *Computer Physics Communications*, Vol. 102, pp. 147–160, 1997.

4. Ushijima, S., Yamada, S., Fujioka, S. and Nezu, I.: Prediction method (3D MICS) for transportation of solid bodies in 3D free-surface flows, *JSCE Journal*, Vol. 810/II-74, pp. 79–89, 2006.

5. Ushijima, S., Fukutani, A., Makino, O. and Nezu, I.: Computational method for arbitrarily-shaped solid models moving in 3D flows with collisions and deformations, *J. Applied Mech., JSCE*, Vol. 10, pp. 139–146, 2007.

6. Brackbill, J. U., Kothe, D. B. and Zemach, C.: A continuum method for modeling surface tension, *J. Comput. Phys.*, Vol. 100, pp. 335–354, 1992.

7. Ushijima, S. and Nezu, I.: Higher-order implicit (C-ISMAC) method for incompressible flows with collocated grid system, *JSCE Journal*, No. 719/II-61, pp. 21–30, 2002.

8. Shin, B. R., Ikohagi, T. and Daiguji, H.: An unsteady implicit SMAC scheme for two-dimensional incompressible Navier-Stokes equations, *JSME International Journal*, Vol. 36, No. 4, pp. 598–606, 1993.

9. Ushijima, S., Yoshida, K., Takemura, M. and Nezu, I.: Fifth-order conservative scheme with flux control applicable to convection equations, *JSCE Journal*, No. 747/II-65, pp. 85–94, 2003.

10. Ushijima, S., Okuyama, Y., Takemura, M. and Nezu, I.: Parallel computational method for pressure field in incompressible flows on 3D curvilinear coordinates, *Annual Journal of Hydraulic Engineering, JSCE*, Vol. 47, pp. 385–390, 2003.

11. Hirt, C. W. and Cook, J. L.: Calculating three-dimensional flows around structures and over rough terrain, *J. Comput. Phys.*, Vol. 10, pp. 324–340, 1972.

12. Vorst, H. A. V. D.: BI-CGSTAB : A first and smoothly converging variant of BI-CG for the solution of nonsymmetric linear systems, *SIAM J. Sci. Stat. Comput.*, Vol. 13, pp. 631–644, 1992.

APPENDIX-NOTATION

The following symbols are used in this paper:

B = width of flume and box;
D = divergence of velocity defined by Eq.23;
$e_{k,ij}$ = deformation tensor of Ω_k;
$\boldsymbol{F}_{Ck}$ = fluid force vector against a tetrahedron element of object k included in a fluid-cell;
F_{Cki} = $i-$component of $\boldsymbol{F}_{Ck}$;
$F_{s,i}$ = acceleration of surface tension in x_i direction;
F_w = fluid force acting on a block model;
F_{wm} = maximum value of F_w;
f = volume fraction of liquid and solid phases in a fluid-cell;
f_b = spatial interpolation function;
f_i = acceleration of external force in x_i direction;
$f_{s,i}$ = acceleration defined by Eq.12;
h_0 = initial water depth;
h_b = height of box;
h_m = maximum water depth;
L_1, L_2 = lengths of experimental flume in Fig.4;
p = volume-averaged pressure;
p_k = pressure of Ω_k;
t = time;
$u_{b,i}$ = cell-boundary velocity component defined by Eq.20;
u_i = mass-averaged velocity component in x_i direction;
$u_{k.i}$ = velocity component of Ω_k in x_i direction;
$\hat{u}_i$ = cell-center velocity component defined by Eq.19;
$\tilde{u}_{k,i}$ = $u_{k,i} - u_i$;
w_h = $h_m - h_b$;
x_i = orthogonal coordinates;
$\alpha,\ \beta$ = parameters ranging $0 \leq \alpha, \beta \leq 1$;
α_k = volume fraction of object k included in a fluid-cell;
ΔC = volume of a fluid-cell;
Δt = time increment;
δ_{ij} = Kronecker's delta;
ϵ_D = threshold for the error on fluid continuity;
μ = volume-averaged coefficient of viscosity;
μ_k = coefficient of viscosity of Ω_k;
ρ = volume-averaged fluid density;
ρ_k = density of Ω_k;
σ_k = density of object k;
τ_{ij} = volume-average of $\tau_{k.ij}$;
$\tau_{k.ij}$ = stress defined by Eq.5;
ϕ = $p^{n+1} - p^n$;
Ω = mixture of fluids; and
Ω_i = fluid component of Ω.

(Received Jul 14, 2008 ; revised Nov 21, 2008)